

A Cumulative Distribution Function Method for Normalizing Variable-Angle Microwave Observations

Nan Ye, Jeffrey P. Walker, and Christoph Rüdiger, *Member, IEEE*

Abstract—Microwave remote sensing has been widely acknowledged as the most promising technique to measure the spatial distribution of near-surface soil moisture. However, due to a strong incidence angle dependence in microwave radiometer and radar data, airborne observations typically have an across-track variation in incidence angle that needs to be normalized to a fixed angle for the purposes of data visualization and aggregation to spatial resolutions that mimic spaceborne data. There are two normalization methods commonly used, often resulting in a noticeable stripe pattern along the flight direction. This paper develops a 2-D cumulative distribution function (CDF)-based normalization method, which normalizes the variable-angle observations to a reference angle by matching the CDF of observations for each nonreference angle, using the information content from multiple partially overlapped swaths. The performance of this method is tested using an airborne microwave radiometer and radar observations collected during three Australian field experiments. The normalization results show that the stripe pattern problem over heterogeneous land surfaces when not any prior knowledge of land surface types is primarily attributed to the linearity of the commonly used normalization methods, and that the nonlinear 2-D CDF-based method produced the least noticeable stripe pattern and the highest normalization accuracy when compared with independent data. Compared with the two linear methods, a root-mean-squared error improvement of up to 2 K was obtained using 1-km radiometer data, and a correlation coefficient improvement of 0.2 and RMSE improvement of ~ 0.2 dB were achieved for the 7-m resolution radar data.

Index Terms—Active and passive microwave remote sensing, incidence angle normalization.

I. INTRODUCTION

DUE to its direct relationship with soil moisture, the ability to penetrate clouds, and the reduced impact by vegetation cover, microwave remote sensing has been widely acknowledged as the most promising technique to measure the high variability of near-surface soil moisture in time and space at regional and global scales [1]–[6]. However, many of the

airborne and spaceborne microwave radiometers and radars used to measure the surface soil microwave emission and backscatter yield a range of across-track viewing angles (e.g., the L-band Push-Broom Microwave Radiometer (PBMR) [7], the Electrically Steered Thinned Aperture Radiometer (ESTAR) [8], the Salinity Temperature And Roughness Remote Scanner (STARSS) [9], the Polarimetric L-band Multibeam Radiometer (PLMR) [10], the Polarimetric L-band Imaging Synthetic Aperture Radar (PLIS) [11], the Cooperative Airborne Radiometer for Ocean and Land Studies (CAROLS) [12], the Advanced Synthetic Aperture Radar [13], and the Phased Array L-band Synthetic Aperture Radar (PALSAR) [14]). Consequently, such observations often need to be normalized to a fixed reference angle for the purpose of visualization, interpretation, and/or simulation of satellite missions, due to the strong sensitivity of microwave signal to incidence angle.

There are two methods widely used for incidence angle normalization, referred to here as the ratio-based [15] and histogram-based [16] methods. Nevertheless, use of these methods over heterogeneous land surfaces has often resulted in a noticeable stripe pattern when producing geo-referenced maps of angle-normalized microwave observations from multiple swaths. It is shown in this study that this striping results (in part) from an assumption of linearity in microwave response across incidence angles. Although the stripe pattern can be reduced by separately applying these methods for each land surface type [16], this is particularly limiting over heterogeneous land surfaces. Consequently, use of a 2-D cumulative distribution function (CDF)-based method is proposed for normalizing variable-angle microwave observations from multiple swaths in order to minimize striping by avoiding the linearity assumption. This approach is based on the CDF matching technique, which has been routinely applied to scaling of remotely sensed observations to modeled soil moisture data [17], establishing relationships between radar reflectivity and rainfall [18], [19], and blending of multiple microwave radiometer-derived soil moisture products [20].

Each of these previous CDF studies has merged two or more data sets by matching their temporal CDFs over the same area based on an assumption of the same temporal variation. In contrast, the 2-D CDF-based incidence angle normalization method developed here is based on matching the spatial CDF of observations measured at each incidence angle. It is assumed that the sorted brightness temperature or backscatter sequence of all observed land surface types is consistent across all incidence

Manuscript received March 19, 2014; revised September 4, 2014; accepted November 17, 2014. This work was supported by the Lake Eyre and AACES campaigns funded by the Australian Research Council under Grant DP0879212 as part of the MoistureMap project, by the SMAPEX campaigns funded by the Australian Research Council under Grant DP0984586, and by the Airborne instruments funded by infrastructure grants of the Australian Research Council under Grant LE0453434 and Grant LE0882509.

The authors are with the Department of Civil Engineering, Monash University, Clayton, VIC 3800, Australia (e-mail: nan.ye@monash.edu; jeff.walker@monash.edu; chris.rudiger@monash.edu).

Digital Object Identifier 10.1109/TGRS.2014.2387574

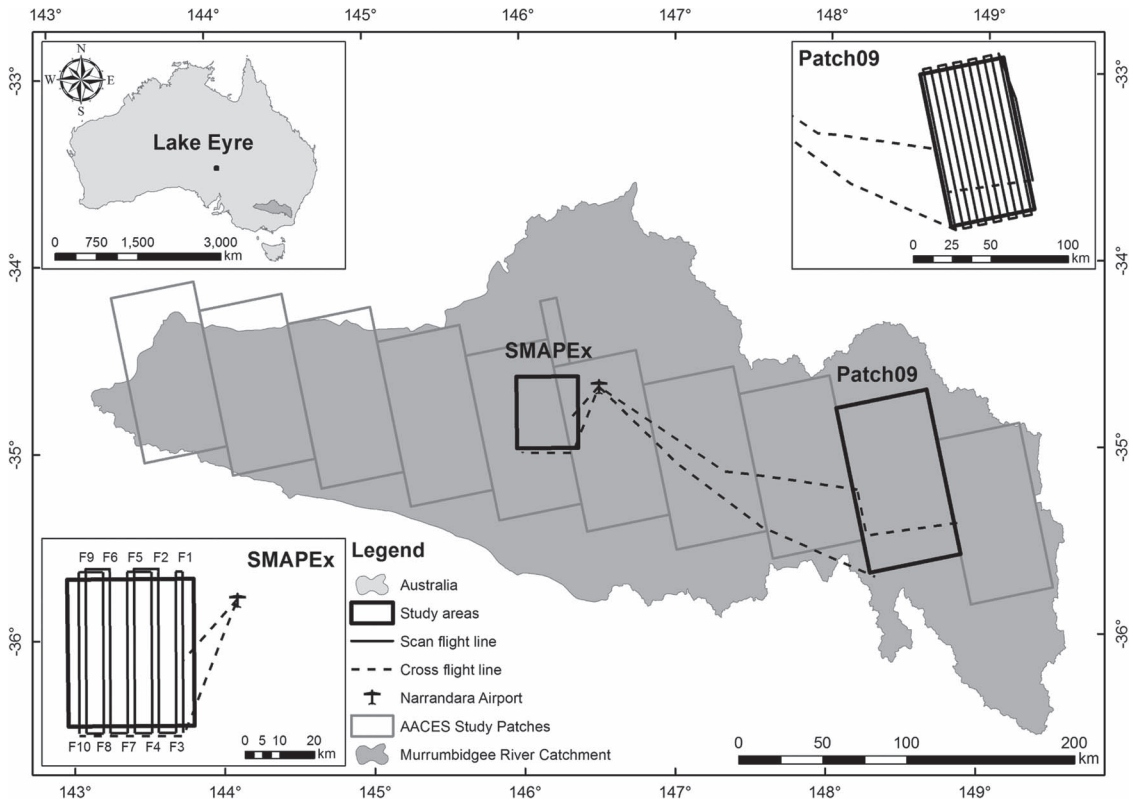


Fig. 1. Location of study areas, flight lines, and transit (cross-) flights used in this study. Transit flights that cross the study area are used for independent verification.

angles. Consequently, for a given land surface, the cumulative frequency is independent of incidence angle and can be used to transfer observations at nonreference angles to the reference angle. However, when the land surface observed at the reference angle is significantly different from that observed at the angle to which it will be normalized, the CDF of the normalized data must be forced to fit that of observations at the reference angle for this approach to be applied without specific consideration of land surface heterogeneity. Accordingly, earlier studies on the normalization of single swath radar backscatter data by Menges *et al.* [21], [22] found a considerable overfitting error in normalized data using the CDF-based method and abandoned the approach [16]. Consequently, the 2-D CDF-based normalization method presented here takes account of this issue by considering the normalized observation difference in the overlapped area of adjacent swaths to force the fit. This new 2-DCDF-based method is tested using a microwave radiometer, and radar observations collected during three airborne field experiments.

II. DATASETS

Airborne microwave radiometer and radar observations collected during three Australian field experiments are used to develop and test the 2-D CDF-based method of this paper. Results are also compared with the two existing normalization methods, both in terms of visual occurrence of stripping and quantitative normalization accuracy when compared with independent data. These experimental data are from the AACES-1 [the first Australian Airborne Cal/val Experiments for Soil Moisture and Ocean Salinity (SMOS) in summer 2010] [23],

the central Australia experiment in summer 2008 [24], and the SMAPEX-3 (the third SMAP Experiments in Spring 2011) [11]. The study locations and flight lines are shown in Fig. 1.

The AACES experiments were designed to provide concurrent radiometric observations with the SMOS [25] mission at the scale of ~ 43 km, for the purpose of SMOS calibration and validation. These experiments (AACES-1 and AACES-2) were conducted over ten 50 km by 100 km flight patches across the Murrumbidgee River catchment in southeast of Australia in January/February, and September of 2010, respectively. The L-band microwave radiometer observations were measured across 19 flight days using the (1.413 GHz) PLMR mounted in push-broom configuration on a scientific aircraft. Both horizontally (H) and vertically (V) polarized brightness temperatures were measured through six across-track beams of the PLMR with viewing angles of $\pm 7^\circ$, 21.5° , and 38.5° from nadir, each having a beam width of 17° along-track and 14° across-track. By flying the aircraft along the designed northwest–southeast flight lines at an altitude of ~ 3000 -m above ground level, brightness temperature observations at 1-km resolution over the entire study area were measured at the three incidence angles. To simulate the brightness temperature observation of SMOS, the variable-angular brightness temperature observations need to be normalized to a fixed angle and integrated over the SMOS pixel-sized areas. While the three normalization methods were applied to all sampled patches, only the brightness temperature observations for Patch 09 on February 18, 2010 are shown in this paper. Results are tested using an independent cross-flight line (see Fig 1), which is from the aircraft transit route back to the airport at the end of the flight.

The central Australia experiment was conducted over central Australia in November 2008 [24]. The main objective was to provide airborne microwave brightness temperature observations at L-band over SMOS-sized areas, which could be used for SMOS on-orbit vicarious calibration [24]. Totally, three 50 km by 50 km areas were sampled using the PLMR with the same configuration as in the AACES. One of the sampled areas, i.e., Lake Eyre, was included as a test area in this paper, since the land surface was characterized by extreme variations in brightness temperature, ranging from ~ 50 to ~ 300 K. This provided an opportunity for an extreme test of the proposed CDF-based normalization method.

The 2-D CDF-based method was also applied to normalization of radar observations collected during the SMAPEX-3. The SMAPEX experiments were conducted over a 36 km by 38 km agricultural area in the Murrumbidgee River catchment (see Fig. 1), which is a test bed of the Soil Moisture Active and Passive (SMAP) mission [26] to develop and validate soil moisture retrieval algorithms using a combined L-band radiometer and radar system. The L-band microwave backscatter observations were collected using the polarimetric L-band (1.26 GHz) imaging synthetic aperture radar (PLIS), whose antennas were mounted on the scientific aircraft with a 30° angle from the horizontal, yielding viewing angles ranging from 15° to 45° on both sides of the flight lines. More than 300 across-track backscatter observations in HH, VV, HV, and VH polarizations were measured within ~ 2 km wide swaths on each side of flight lines, resulting in a spatial resolution of ~ 7 m. Consequently, backscatter data were obtained over the entire SMAPEX-3 study area from ten consecutive north-south flight lines (F1 to F10) resulting in a total of 20 swaths. Each swath was partially overlapped with adjacent swaths in order to provide a full coverage over the study area. Since the SMAP is designed to operate in a conical scan mode with a fixed incidence angle of 40° , the PLIS backscatter data collected at variable incidence angles need to be normalized to the SMAP incidence angle. In this paper, the HH polarized backscatter data collected on September 15, 2011 is used as an example to test the performance of the CDF-based normalization method on radar data.

III. NORMALIZATION METHODS

The normalization function is an approximation of the corresponding relationship between the observations at an incidence angle and what would be observed at a given reference angle over the same pixels. Two commonly used normalization methods exist in the literature: the ratio-based [15] and histogram-based [16] methods. The ratio-based method was initially used to normalize multibeam brightness temperature at any observed incidence angle (θ_{obs}) to the reference angle (θ_{ref}), expressed as

$$\Omega_{norm} = \Omega_{obs} \cdot \frac{\bar{\Omega}_{ref}}{\bar{\Omega}_{obs}} \quad (1)$$

where Ω represents radiometer brightness temperature TB or radar backscatter σ observation hereafter in this paper. The Ω_{obs} and Ω_{norm} are the observed microwave observation and its normalized value, whereas $\bar{\Omega}_{obs}$ and $\bar{\Omega}_{ref}$ indicate the mean

values of all observations at θ_{obs} and θ_{ref} , respectively. The histogram-based normalization method was developed for the incidence angle normalization of radar backscatter observations by also accounting for the standard deviations of backscatter observations at each incidence angle step. The normalized observation in the histogram-based method is determined by

$$\Omega_{norm} = \bar{\Omega}_{ref} + \hat{\Omega}_{ref} \cdot \frac{\Omega_{obs} - \bar{\Omega}_{obs}}{\hat{\Omega}_{obs}} \quad (2)$$

where $\hat{\Omega}_{obs}$ and $\hat{\Omega}_{ref}$ indicate the standard deviations of all observations at θ_{obs} and θ_{ref} , respectively. Additionally, the CDF-based method used for normalizing the backscatter data from a single swath in the earlier studies of Menges *et al.* [21], [22] normalized the original observation Ω_{obs} to the observation at the reference angle Ω_{ref} with the same cumulative probability as Ω_{obs} , such that

$$cdf_{ref}(\Omega_{norm}) = cdf_{obs}(\Omega_{obs}) \quad (3)$$

where cdf_{ref} and cdf_{obs} are CDFs of observations at the reference angle and the angle to be normalized, which can be calculated by sorting the observations for each incidence angle step. As for the ratio-based and histogram-based methods, the CDF-based normalization method assumes that the full cross-section of land surface conditions was observed at all incidence angles. However, the land surface composition of the fields viewed by the reference angle can be different from that of the other angles, such that (3) will force the CDF of normalized observations at all incidence angles to overfit that at the reference angle, and induce a nonnegligible error in the normalized data [16].

It can be noticed that both the ratio-based and histogram-based normalization functions are linear between the original observations (Ω_{obs}) and their normalized values (Ω_{norm}). While this linear assumption may be satisfied over homogeneous land surfaces, since the angular relationship of land surface components over homogeneous land surfaces are the same or parallel to each other, the observations at a specific incidence angle linearly correspond to those observed from a different angle over the same area. However, it may not be reasonable over highly heterogeneous land surfaces. Consequently, in the absence of using land surface classification information, a noticeable stripe pattern has been observed from multiple swath data when using linear normalization methods over inhomogeneous land surfaces, as shown in the left plots of Fig. 4. This study hypothesizes that the relationship between microwave observations at different incidence angles is nonlinear over a heterogeneous terrain, and that the linear normalization methods are responsible for the stripe pattern in maps of normalized observations (see Figs. 4 and 6). Accordingly, a nonlinear 2-D CDF-based normalization method is proposed to deal with the stripe pattern and overfitting problems for microwave observations collected from multiple partially overlapped swaths.

In the 2-D CDF-based normalization method, a CDF cdf_i of incidence angle $\theta_{obs,i}$ and microwave observation $\Omega_{obs,i}$ can be established for each swath i as according to $cdf_i(\theta_{obs,i}, \Omega_{obs,i})$. The variation of microwave observations between incidence

angles is considered as the combined effect of the microwave angular response over the same land surface and land surface heterogeneity between fields of view, where the former effect is assumed similar across swaths, and the latter is assumed independently random. By averaging the cdf_i across swaths, the effect of land surface heterogeneity on the corresponding relationship can be reduced, with only the angular effect retained in the mean CDF \overline{cdf} of all swaths. In addition, as the angular relationship of microwave observations is a continuous smooth curve over the same area, the \overline{cdf} was further smoothed in the dimension of incidence angle using a moving average filter, and the smoothed function \overline{cdf}_{smooth} taken as the normalization equation, according to

$$\overline{cdf}_{smooth}(\theta_{ref}, \Omega_{norm,i}) = \overline{cdf}_{smooth}(\theta_{obs,i}, \Omega_{obs,i}) \quad (4)$$

where $\Omega_{norm,i}$ is the normalized observation of $\Omega_{obs,i}$ at the incidence angle of $\theta_{obs,i}$ in Swath i .

For instruments with a small number of beams and a big beamwidth, such as the PLMR having three beams with a beamwidth of $\sim 15^\circ$ on each side of the aircraft, the observations of the entire study area are collected at three discrete viewing angles. Over a study area, a big part (about one-third) of the area can be observed at each viewing angle, and all land cover types are typically collected from all viewing angles. Consequently, the land surface conditions of the study area viewed at each viewing angle can be assumed representative to the entire study area and also similar between each other. In this case, the similar land surface assumption of the CDF-based normalization method can be satisfied, and (4) can be applied to normalize the observations with a reasonable reliability. However, for instruments with a large number of beams of narrow beamwidth, such as the PLIS having over 300 azimuthal beams within the incidence angles range of 15° to 45° , the land surfaces viewed by these very fine beams are generally inhomogeneous between incidence angles, and not all types of land cover responses are captured by each beam and swath. Thus, the land surface heterogeneity of field view between incidence angles and swaths should also be considered during the normalization. If (4) is directly applied in this case, the CDF of original observations at each incidence angle step has been found to overfit to the \overline{cdf}_{smooth} at the reference angle. As a result, the natural land surface feature is removed and a significant difference can be found over the overlapped area of adjacent normalized images. Therefore, a modification to (4) is proposed for sensors with a large beam number, which will retain the effect of land surface heterogeneity. Accordingly, (4) is used to prenormalize the first-order angular effect, with the remaining second-order angular effects corrected by minimizing the difference of prenormalized observations in the overlapped areas of adjacent swaths. Due to the heterogeneity between swaths, the second-order angular effect correction is specifically undertaken for each swath, with a 2-D polynomial function Δcdf_i used to correct \overline{cdf}_{smooth} for swath i according to

$$\Delta cdf_i(\theta_{obs,i}, \Omega_{obs,i}) = \sum_{a=0}^{m-1} \sum_{b=0}^{n-1} A_{a,b,i} \cdot \Omega_{obs,i}^a \cdot \theta_{obs,i}^b \quad (5)$$

where $A_{a,b,i}$ is a m by n coefficient matrix for a th power of observation $\Omega_{obs,i}$ and b th power of incidence angle $\theta_{obs,i}$ for swath i . The values of m and n determine the freedom of Δcdf_i in dimensions of observation and incidence angle. The higher the value used, the better the fit between swaths obtained, but the probability of inducing larger normalization error also increases. A default value of 4 is suggested for both m and n in general cases. The $A_{a,b,i}$ is determined by fitting the CDF of normalized observations in the overlapped area of each pair of adjacent swaths, according to

$$\overline{cdf}_{smooth}(\theta_{obs,i}, \Omega_{obs,i}) + \Delta cdf_i(\theta_{obs,i}, \Omega_{obs,i}) = \overline{cdf}_{smooth}(\theta_{obs,j}, \Omega_{obs,j}) + \Delta cdf_j(\theta_{obs,j}, \Omega_{obs,j}) \quad (6)$$

where subscripts i and j indicate adjacent swaths. The left part of (6) is the CDF of a normalized observation at the incidence angle of $\theta_{obs,i}$ in swath i , whereas the right part is that of the same pixel in swath j with incidence angle of $\theta_{obs,j}$. The coefficient matrices $A_{a,b,i}$ of all swaths can be obtained simultaneously using an iterative optimization by satisfying (6) for all adjacent swaths pair. Consequently, (4) is modified for swath i using Δcdf_i with the optimized $A_{a,b,i}$, according to

$$\overline{cdf}_{smooth}(\theta_{ref}, \Omega_{norm,i}) + \Delta cdf_i(\theta_{ref}, \Omega_{norm,i}) = \overline{cdf}_{smooth}(\theta_{obs,i}, \Omega_{obs,i}) + \Delta cdf_i(\theta_{obs,i}, \Omega_{obs,i}). \quad (7)$$

IV. VERIFICATION USING SYNTHETIC DATA

This section explores the normalization function linearity and the theoretical accuracy of all three normalization methods using synthetic microwave radiometer observations over a consistent type of land surface. To satisfy the similar land surface assumption, a 500 by 500 grid was generated to simulate brightness temperature observations over a native grass surface. It was assumed that odd and even columns of the grid were taken as the reference columns observed at the incidence angle of 38.5° (θ_{ref}) and test columns at the incidence angle of 21.5° (θ_{obs}), respectively, with the intention to normalize the brightness temperature at the nonreference angle to the reference angle using each of the three normalization methods. The L-MEB [27], [28] model was used to simulate dual-polarized brightness temperatures of each pixel at the predetermined incidence angle ($T_{B_{ref}}$ for the reference columns and $T_{B_{obs}}$ for the test columns). For the purpose of this demonstration, the brightness temperature of the test columns were also simulated at the reference angle (θ_{ref}), and subsequently used as the ‘‘truth’’, referred as $T_{B_{norm}^*}$ for evaluating the three normalization methods.

The L-MEB model is the basis for the SMOS Level 2 retrieval algorithm, which retrieves soil moisture and vegetation water content simultaneously from dual-polarized brightness temperature observations by minimizing the differences between observed and simulated brightness temperature using the $\tau - \omega$ model [29]. According to the $\tau - \omega$ model, the microwave emission from a vegetated soil surface is defined as the sum of: i) the upward radiation from the vegetation layer; ii) the downward radiation from the vegetation layer reflected by the soil surface and attenuated by the vegetation layer; and

TABLE I
LAND SURFACE PARAMETERS USED IN THE L-MEB (AFTER [10])
FOR DERIVING THE SYNTHETIC VERIFICATION DATA SET

Soil moisture	0 – 0.6-m ³ /m ³	Vegetation structure tt_h	1
Vegetation water content	0 – 2-Kg/m ²	Vegetation structure tt_v	1
Roughness H_R	0 – 0.6	Vegetation parameter b	0.15
Sand content	67%	Scattering albedo ω_h	0
Clay content	15%	Scattering albedo ω_v	0.05
Bulk density	1.1-g/cm ³	Surface soil temperature	300-K
Roughness N_{Rh}	0	Deep soil temperature	292-K
Roughness N_{Rv}	0	Vegetation temperature	300-K

iii) the upward radiation from the soil layer attenuated by the vegetation layer. Thus

$$TB_p = (1 - \omega_p) \cdot (1 - \gamma_p) \cdot (1 + \gamma_p \Gamma_p) \cdot T_v + (1 - \Gamma_p) \cdot \gamma_p \cdot T_s \quad (8)$$

where T_v and T_s are the effective vegetation and soil temperatures [K]. ω_p and γ_p are the single scattering albedo and transmissivity of the vegetation layer, and Γ_p is the reflectivity of a rough soil surface. Subscript p refers to the polarization (either horizontal or vertical). The transmissivity of the vegetation layer γ_p is a function of the vegetation optical depth at nadir τ_{NAD} , the vegetation structure parameter tt_p , and the incidence angle θ , given by

$$\gamma_p = \exp \left[-\tau_{NAD} \cdot (tt_p \cdot \sin^2(\theta) + \cos^2(\theta)) \cdot \cos^{-1}(\theta) \right] \quad (9)$$

where the vegetation optical depth at nadir τ_{NAD} is assumed to be the product of the vegetation water content and parameter b [30], [31]. The reflectivity of a rough soil surface Γ_p is dependent on the roughness parameters H_R and N_{Rp} [28], [32] according to

$$\Gamma_p = \Gamma_p^* \cdot \exp \left[-H_R \cdot \cos^{N_{Rp}}(\theta) \right] \quad (10)$$

as a function of the incidence angle θ and the smooth soil surface reflectivity Γ_p^* , which can be calculated through the Fresnel equations. In this paper, the Dobson *et al.* [33] mixing model was used to estimate the relative dielectric constant of the soil, a main input in the Fresnel equations, from information about soil water content, soil texture, and soil bulk density.

The heterogeneous grass land surfaces were simulated by randomly assigning soil moisture, vegetation water content, and roughness parameter H_R of each pixel of the 500 × 500 grid within the typical ranges. The ranges and values of other parameters for natural grass land surfaces required by the L-MEB are listed in Table I. For the test columns, the simulated brightness temperature observations (TB_{obs}) against the truth of normalized observation (TB_{norm}^*) are plotted together with curves of the three normalization functions in Fig. 2. It can be clearly seen that TB_{obs} has a nonlinear relationship to TB_{norm}^* for both horizontal and vertical polarizations, confirming that the hypothesis of a nonlinear transformation requirement for incidence angle normalization is correct over the same type of land surface with heterogeneous soil moisture, vegetation water content, and surface roughness distribution. Consequently, a nonlinear normalization method should be used for general

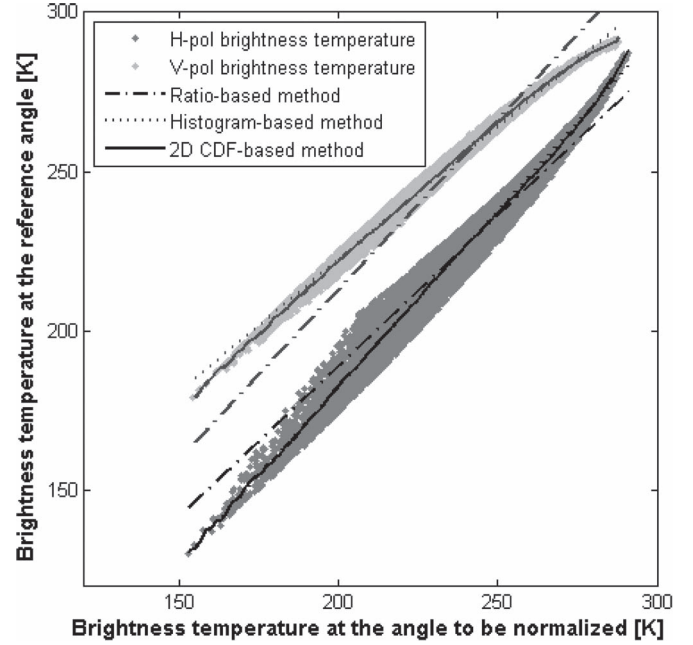


Fig. 2. Comparison of brightness temperatures observed at the incidence angle of 21.5° (◊) against the truth data at the reference incidence angle of 38.5° (◊) from the synthetic experiment. Results are for the three normalization methods tested.

heterogeneous land surfaces, even for a single land surface type such as when using a land surface classification. To quantify the accuracy of the three normalization methods, two best-fit fifth-order polynomial curves to the relationships between TB_{obs} and TB_{norm}^* were used as the best possible normalization function scenario for horizontal and vertical polarizations, respectively. However, due to the integrated effect of soil moisture, vegetation water content, and surface roughness on the angular relationship, the TB_{obs} versus TB_{norm}^* plot shows a scattering around the truth curves with a standard deviation of a few kelvins, demonstrating the theoretical uncertainty of normalization methods. While all three methods fit the main trend of the truth of normalized brightness temperature in Fig. 2, it can be seen from the difference between TB_{norm} and TB_{norm}^* in Fig. 3 that errors as large as 10 K were observed at the warm and cool ends of the observations. It is this large difference that results in the striping pattern in geo-referenced brightness temperature maps. In contrast, the 2-D CDF-based method was able to achieve an error of less than 3 K for H polarization and 1 K for V polarization across the whole range of brightness temperatures simulated.

To further quantify the accuracy of all three normalization methods under diverse soil moisture, vegetation water content, and surface roughness conditions, the bias and root-mean-squared error (RMSE) was calculated for the entire grid by comparing the truth observations (TB_{norm}^*) with the normalized observations (TB_{norm}). To minimize any impact from the synthetic experiment design, the analysis was repeated for 20 realizations of soil moisture, vegetation water content, and surface roughness conditions. The mean (μ) and standard deviation (σ) of the bias and RMSE in all 20 realizations were calculated and are listed in Table II. The 2-D CDF-based method had a mean RMSE of 2.64 K in horizontal polarization

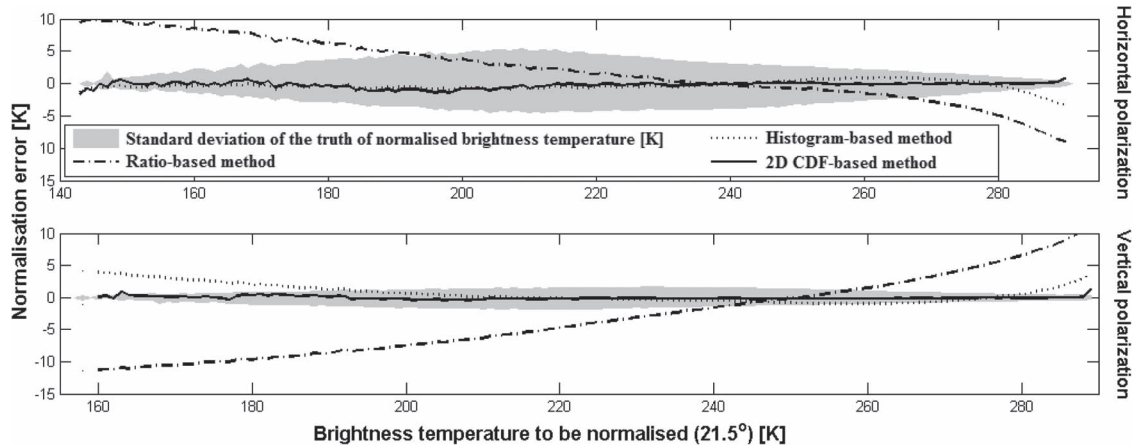


Fig. 3. Mean and standard deviation of error in normalized brightness temperature according to brightness temperature value for each of the three normalization methods. Results are from the synthetic experiment when normalizing from 21.5° to 38.5°.

TABLE II
BIAS AND RMSE OF THE THREE NORMALIZATION METHODS WHEN USING A SYNTHETIC DATA SET OF BRIGHTNESS TEMPERATURES [K]. THE MEAN (μ) AND STANDARD DEVIATION (σ) OF TB BIAS AND RMSE FOR 20 REPLICATES ARE ALSO GIVEN. THE BEST-FIT POLYNOMIAL RESULTS PROVIDE THE THEORETICAL BEST BENCHMARK

		Ratio-based method	Histogram-based method	2D CDF-based method	Best-fit polynomial
		$\mu(\sigma)$	$\mu(\sigma)$	$\mu(\sigma)$	$\mu(\sigma)$
Horizontal polarization	Bias	-0.008 (0.151)	-0.008 (0.151)	-0.008 (0.152)	0.000 (0.000)
	RMSE	3.764 (0.023)	2.722 (0.006)	2.643 (0.006)	2.643 (0.004)
Vertical polarization	Bias	-0.009 (0.113)	-0.009 (0.113)	-0.009 (0.113)	0.000 (0.000)
	RMSE	3.914 (0.012)	1.187 (0.007)	0.941 (0.007)	0.931 (0.002)

and 0.93 K in vertical polarization under the tested land surface conditions, which closely approximated the theoretical maximum accuracy shown previously. The small bias implies that an insignificant error may be induced when aggregating the whole grid of observations to one single pixel value.

V. VERIFICATION USING MICROWAVE RADIOMETER OBSERVATIONS

The capacity of the 2-D CDF-based method to deal with the striping problem was further verified using airborne brightness temperature data collected over Patch 09 during an ~5-h flight in the AACES-1 experiment. Over each patch during the AACES experiments, about 12 km of the first flight line was repeated at the end of the flight in order to assess the temporal variation of brightness temperature observations, which was up to 5 K. This variation was corrected by multiplying the ratio of effective soil temperature at the SMOS nominal overpass time of 6 A.M. (local time) to that at the time of each observation. The effective temperature was derived from a time series of top 5-cm soil moisture and physical temperature at 2.5-cm and 40-cm soil depth, which were measured and recorded by temporal monitoring stations installed in each patch during the

sampling [23]. After the temporal correction, the brightness temperature difference for the repeat flight line was reduced to ~1 K, implying a negligible temporal impact compared with the SMOS radiometric sensitivity of 3.95 K [25].

After temporal correction, brightness temperature observations collected during the mapping flight at incidence angles 7°, 21.5°, and 38.5° with an across-track beamwidth of 7.5° were normalized to the reference angle of 38.5° using the three different methods. Due to a small number of viewing angles of the PLMR, the land surface of fields viewed by each beam is assumed to be representative of the entire study area, and thus (4) was used in the 2-D CDF-based normalization method. The normalized brightness temperature observations were then mapped to a 1-km grid using the “drop-in-bucket” technique, as shown in Fig. 4. Compared with the two linear normalization methods, it can be clearly seen that the 2-D CDF-based method was minimally affected by striping.

To independently verify the angular normalized brightness temperatures, results were compared with the brightness temperature observations measured by the PLMR outer beams (being the 38.5° reference angle) on either side of the flight track during the transit flights that crossed the Patch 9 study area, as shown in Fig. 4. The normalized brightness temperature observations from the mapping flight are compared with the direct observations from the crossing flights over the same pixels in Fig. 5. Amongst the three methods, the 2-D CDF-based approach had the highest accuracy with a RMSE of 4.02 K in horizontal polarization and 2.68 K in vertical polarization, under the land surface condition of Patch09 during the AACES-1. Similar results were obtained over other study patches during the AACES-1 and AACES-2, such that up to 5 K improvement on RMSE was achieved by using the 2-D CDF-based method over other methods. It can be seen that the 2-D CDF-based method improvements on the normalization accuracy were generally higher in V polarization than in H polarization due to the increased nonlinearity of angular relationship in V polarization, as shown in Fig. 2.

Airborne variable-angle brightness temperature observations over the Lake Eyre were also normalized to the reference angle of 38.5° using all three methods individually. Fig. 6 shows the

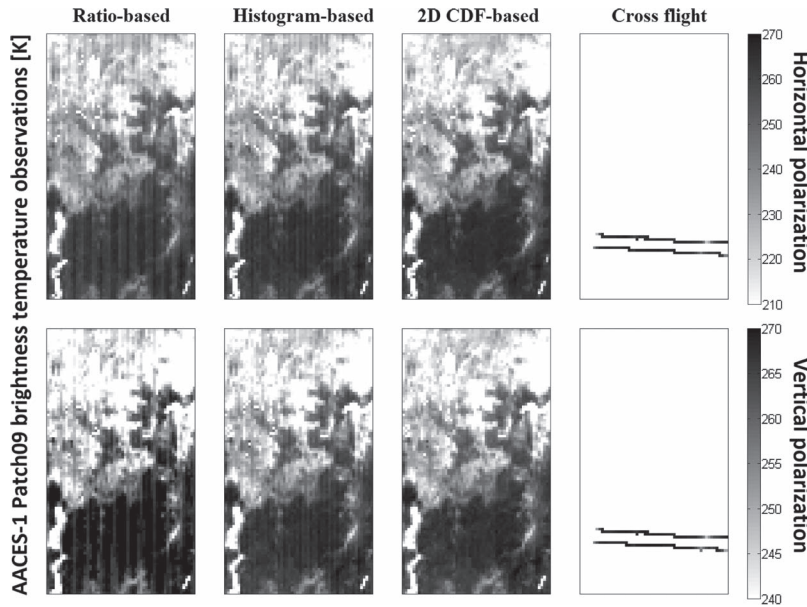


Fig. 4. Brightness temperature maps [K] of AACES-1 Patch09 at H (top) and V (bottom) polarization, normalized to the reference angle (38.5°) using the three normalization methods. Also shown is the directly observed brightness temperature observations from the cross flight used for independent verification.

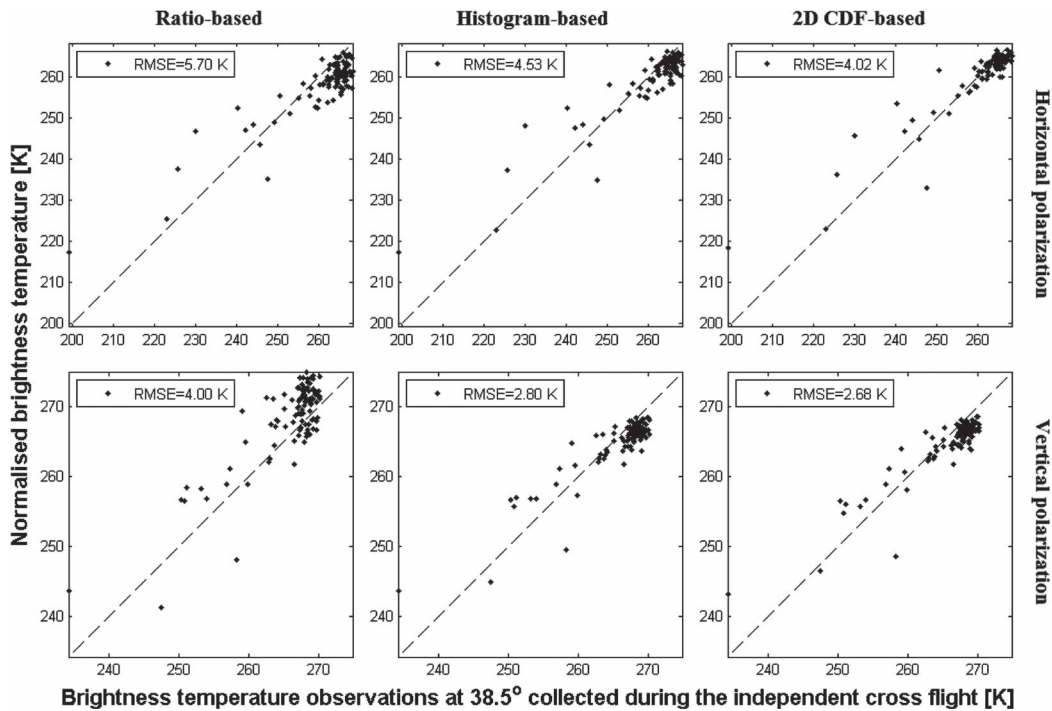


Fig. 5. Comparison between directly observed cross-flight brightness temperature at 38.5° and normalized scan-flight brightness temperature of Patch 9 in the AACES-1, as shown in Fig. 4.

normalized brightness temperature data and the original observations collected from the reference incidence angle during the cross flight. Due to the land surface conditions at the time data were collected over the Lake Eyre being characterized by a hyper saline salt pan with supersaturated highly organic material and dry silty material with low salt content, the observed brightness temperature ranged from 50 to 300 K. It is clear in Fig. 6 that the brightness temperature observations normalized using linear methods retain a significant stripe pattern along

the north–south flight direction, whereas the 2-D CDF-based method results in a much better visual performance. The accuracy of normalization methods was quantified by comparing normalized data to the cross-flight observations of individual pixels made at the respective incidence angle. Taking the cross-flight observations as the truth, the three panels of Fig. 7 illustrate the true brightness temperature versus the normalized value for each pixel using all three normalization methods. The RMSE of each method was calculated, showing that the 2-D

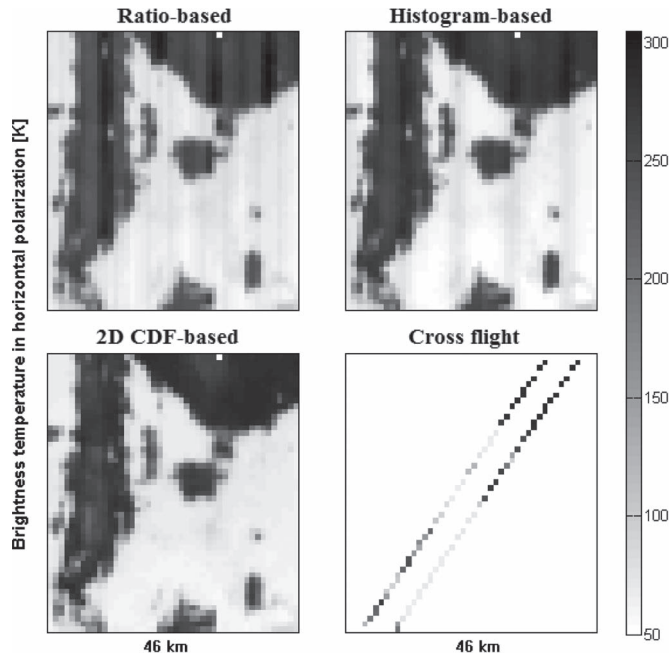


Fig. 6. Brightness temperature maps [K] of Lake Eyre at H polarization, normalized to the reference angle (38.5°) using the three normalization methods, and directly observed brightness temperature observations from the cross flight used for independent verification.

CDF-based method had an improvement of ~ 2 K in accuracy, as compared with the ratio-based and histogram-based methods, in addition to the more pleasing visual characteristics.

VI. VERIFICATION USING RADAR OBSERVATIONS

In this paper, the 2-D CDF-based normalization method (7) was tested using the HH polarized PLIS data collected from 20–2-km wide swaths (left and right swaths of ten flight lines) over the entire study area of the SMAPEX-3 experiment. Due to the almost full overlap of the left swaths of the sixth and seventh flight lines (F6 and F7), normalized backscatter observations in the left swath of F7 were retained as independent data to evaluate the accuracy of normalization methods applied to F6 and the remaining 18 swaths, which can still make a full coverage over the SMAPEX-3 study area. The backscatter data were normalized to the midswath viewing angle of 30° using the three normalization methods, respectively, and the normalization applied to the entire swath without using land surface classification information.

Fig. 8 shows the 2-D CDF of original observations σ_{obs} , the smoothed mean CDF of backscatter observations over all 19 swaths (\overline{cdf}_{smooth}), the CDF of prenormalized observations $\sigma_{pre-norm}$ using (4), and that of the normalized observations (σ_{norm}) over the left swath of F6. It is clear that the CDF of $\sigma_{pre-norm}$ varies with incidence angle and in response to land surface heterogeneity. The rough pattern seen in the CDF of raw observations is the signature of land surface heterogeneity in the given swath. Applying (4) using \overline{cdf}_{smooth} [see Fig. 8(b)], the angular impact was corrected while maintaining the heterogeneous land surface signature in the CDF of $\sigma_{pre-norm}$ [see Fig. 8(c)]. In this paper, 4 by 4 coefficient matrices A were

used with $\sigma_{pre-norm}$. According to Fig. 8(c) and (d), the CDF of optimized σ_{norm} had a small difference to that of $\sigma_{pre-norm}$, confirming that \overline{cdf}_{smooth} is the general angular relationship. Thus, (4) can correct the primary angular impact on microwave observations and has a sufficient accuracy for sensors with a small number of beams.

The normalized backscatter observations over the left swaths of F6 and the adjacent left swath of F8 are taken as an example to demonstrate the performance of the 2-D CDF-based method on stripe removal in radar data. As shown in Fig. 9(e), backscatter observations in the left swath of F6 and F8 have a mean difference of 7.3 dB within their overlapped area before correcting for incidence angle, and more than 90% of overlapped pixels had backscatter differences larger than 4 dB. After applying the 2-D CDF-based normalization method, the mean difference reduced to 2.1 dB, with 90% of pixels having differences less than 4 dB, as shown in Fig. 9(f). However, the backscatter of furrowed areas [very bright areas mostly in the top left of Fig. 9(b)] has a considerable sensitivity on, and an unpredictable relationship to, incidence angle, making it much higher than natural land surfaces at low incidence angles. Consequently, this unusual angular relationship results in ~ 25 -dB difference between the adjacent swaths when using the 2-D CDF-based normalization method. The result also implies that land surface classification data are required to improve the accuracy of radar incidence angle normalization, as the study of Mladenova [16].

To further evaluate the accuracy of the 2-D CDF-based method, the backscatter observations collected at the reference angle of 30° in the left swath of F7 were taken as the truth, and compared with normalized backscatter data using the three methods individually, over the overlapped pixels in the left swath of F6, as shown in Fig. 10. The correlation coefficient (R) and RMSE between the independent reference and normalized observations were calculated for each method. The RMSE of all three methods was 4.44 dB for the ratio-based method, 4.52 dB for the histogram-based method, and 4.26 dB for the 2-D CDF-based method. While the RMSE for the 2-D CDF-based method was only ~ 0.2 dB lower than the linear methods, there was a much larger impact in terms of correlation coefficient. The 2-D CDF-based method had the highest R of 0.73, with only 0.53 for the ratio-based and histogram-based methods. Similar conclusions were drawn from normalization results of the PLIS observations in other polarization configurations, sampling day, and reference angle between 15° to 45° .

VII. CONCLUSION

The radiometer and radar instruments working at microwave frequency were widely used to measure soil moisture in the top few centimeters. Due to the sensitivity of microwave signals to incidence angle, microwave data measured by push-broom instruments having a wide range of incidence angles often need to be normalized to a single reference angle. However, the two commonly used methods typically suffer from a striping problem when applied over heterogeneous land surfaces due to their linear approximation assumptions. Consequently, a nonlinear normalization method was developed for observations collected

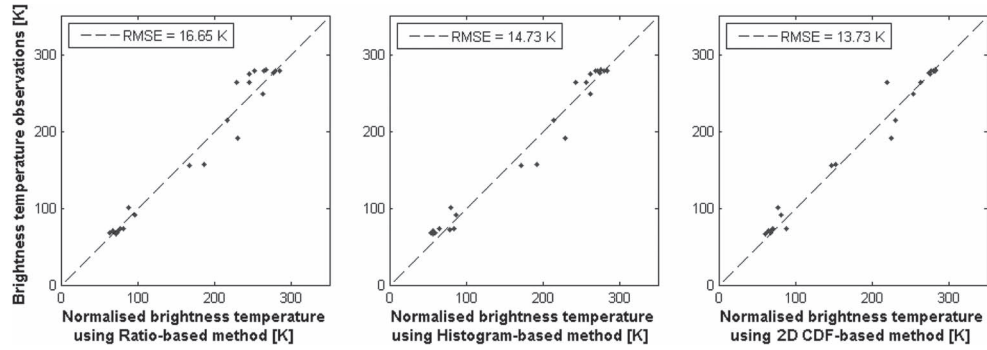


Fig. 7. Comparison between directly observed cross-flight brightness temperature at 38.5° and normalized scan-flight brightness temperature of Lake Eyre, as shown in Fig. 6.

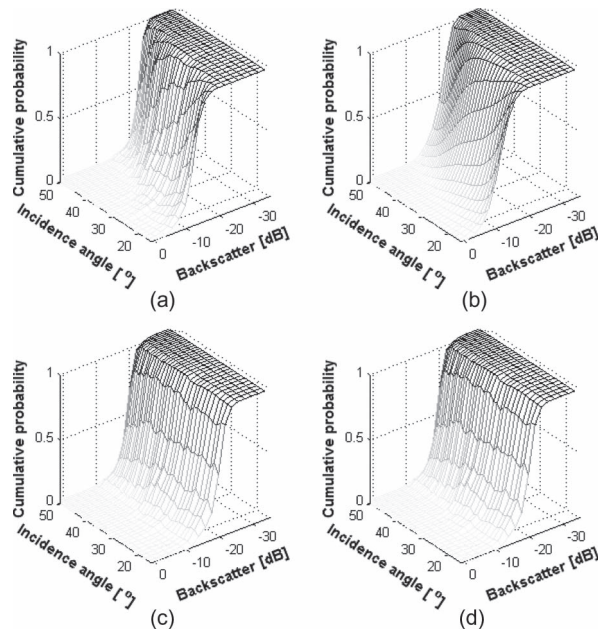


Fig. 8. (a) The CDF of backscatter observations over the left swath of the sixth flight line (F6) at HH polarization on September 23, 2011 during the SMAPEX-3; (b) the smoothed mean CDF of PLIS backscatter for all 20 swaths observed; (c) the prenormalized CDF of (a) using (b); and (d) the adjusted (c) by comparing with adjacent swaths.

from multiple swaths and tested in this study using L-band airborne radiometer and radar observations collected during three Australian field experiments. This method was based on the CDF approach, which normalizes variable-angle observations by matching the CDF of data viewed at nonreference angles. When applied to narrow beam observations, the effects of land surface heterogeneity and the overfitting problem identified in earlier literature were reduced by considering the observation difference in the overlapped area of adjacent swaths. Therefore, this 2-D CDF-based method can only be applied to observations with partially overlapped swaths.

According to a synthetic study on microwave radiometer observations, the RMSE of current normalization methods is limited to between 2 and 13 K depending on polarization and land surface condition. The 2-D CDF-based normalization method had the lowest RMSE in the three methods, with an accuracy that is close to the theoretical minimum. When verified on real microwave radiometer observations, the 2-D

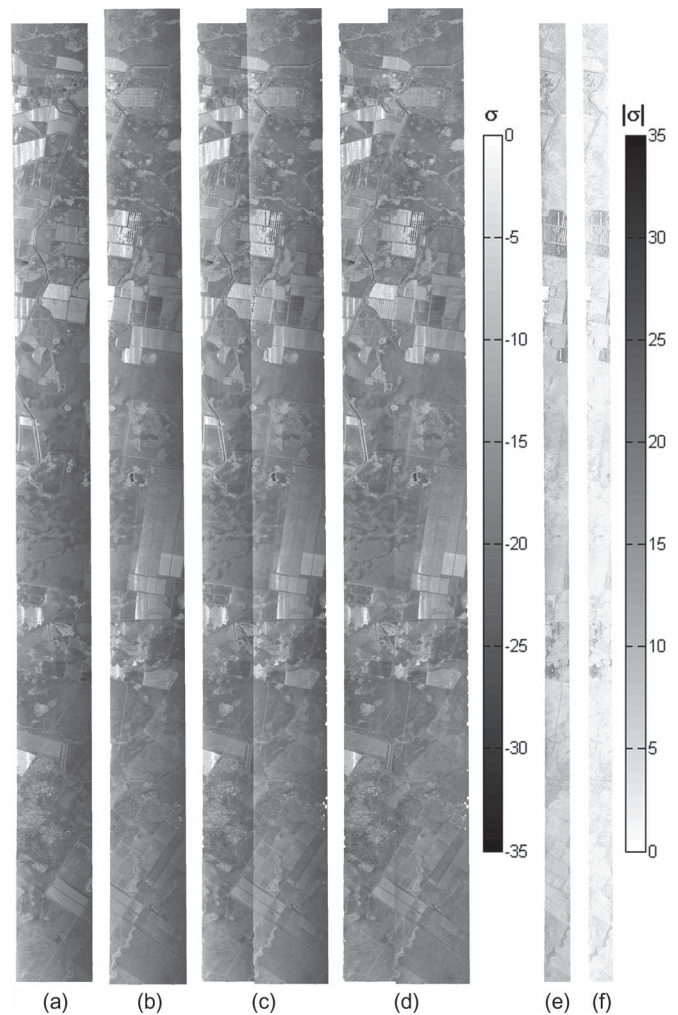


Fig. 9. PLIS backscatter [dB] at HH polarization observed on September 23, 2011 during the SMAPEX-3 over (a) the left swath of the eighth flight line F8 and (b) the left swath of the sixth flight line F6; (c) combined image of (a) and (b) showing incidence angle induced variations; (d) combined image of angle normalized (a) and (b) using the CDF-based method; and absolute difference between the two swaths in their overlapped area (e) before normalization and (f) after normalization.

CDF-based method had the least stripping and the highest or second highest accuracy with a RMSE improvement of up to 2–5 K over the existing linear normalization methods, when compared with independent reference data collected in transit

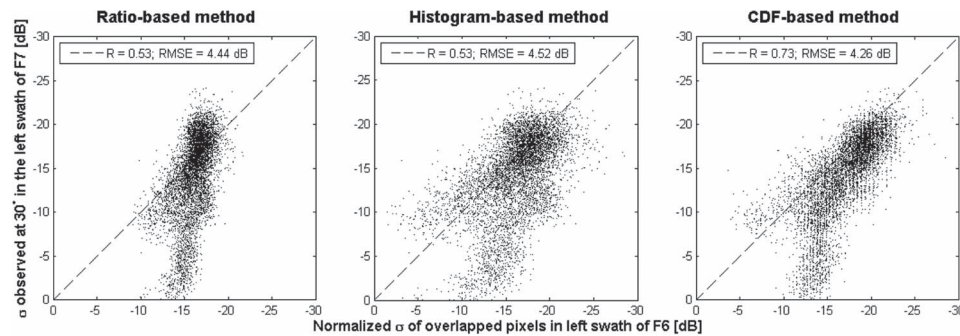


Fig. 10. Comparison between HH polarized backscatter observed at 30° incidence angle in the left swath of F7 and normalized backscatter of the overlapped pixels in the left swath of F6 using the three normalization methods, respectively.

flights under diverse land surface conditions. In the context of the SMOS brightness temperature error budget of 3.95 K, this improvement is significant when simulating spaceborne observations over heterogeneous land surfaces. Verification with radar data over two partially adjacent swaths produced a normalized backscatter correlation coefficient of 0.73 and RMSE of 4.26 dB for the 2-D CDF-based method when compared with independent data with an improvement of 0.2 and 0.2 dB from the other methods, which is significant for soil moisture retrieval and downscaling algorithm applications. However, a difference of up to 25 dB remained over furrowed surfaces, due to inconsistent backscatter responses from mixed furrow areas.

ACKNOWLEDGMENT

The authors would like to thank Dr. R. Panciera and Dr. M. Tanase from the Cooperative Research Centre for Spatial Information, University of Melbourne, Australia for providing the calibrated and georegistered polarimetric L-band imaging synthetic aperture radar data used as one of the examples in this paper, and for constructive discussion.

REFERENCES

- [1] H. Gao, E. Wood, T. Jackson, M. Drusch, and R. Bindlish, "Using TRMM/TMI to retrieve surface soil moisture over the southern United States from 1998 to 2002," *J. Hydrometeorol.*, vol. 7, pp. 23–38, Feb. 2006.
- [2] M. McCabe, H. Gao, and E. Wood, "Evaluation of AMSR-E-derived soil moisture retrievals using ground-based and PSR airborne data during SMEX02," *J. Hydrometeorol.*, vol. 6, no. 6, pp. 864–877, Dec. 2005.
- [3] E. G. Njoku, T. J. Jackson, V. Lakshmi, T. K. Chan, and S. V. Nghiem, "Soil moisture retrieval from AMSR-E," *IEEE Trans. Geosci. Remote Sens.*, vol. 41, no. 2, pp. 215–229, Feb. 2003.
- [4] M. Owe, R. de Jeu, and T. Holmes, "Multisensor historical climatology of satellite-derived global land surface moisture," *J. Geophys. Res., Earth Surface*, vol. 113, no. F11, pp. 1–17, Mar. 2008.
- [5] W. Wagner *et al.*, "Evaluation of the agreement between the first global remotely sensed soil moisture data with model and precipitation data," *J. Geophys. Res., Atmos.*, vol. 108, no. D19, pp. 1–17, Oct. 2003.
- [6] J. Wen, Z. Su, and Y. Ma, "Determination of land surface temperature and soil moisture from tropical rainfall measuring mission/microwave imager remote sensing data," *J. Geophys. Res., Atmos.*, vol. 108, no. D2, pp. ACL 2-1–ACL 2-10, Jan. 2003.
- [7] J. Wang, J. C. Shiue, T. Schmugge, and E. T. Engman, "The L-band PBMR measurements of surface soil moisture in FIFE," *IEEE Trans. Geosci. Remote Sens.*, vol. 28, no. 5, pp. 906–914, Sep. 1990.
- [8] D. M. Le Vine, M. Kao, A. B. Tanner, C. T. Swift, and A. Griffiths, "Initial results in the development of a synthetic aperture microwave radiometer," *IEEE Trans. Geosci. Remote Sens.*, vol. 28, no. 4, pp. 614–619, Jul. 1990.
- [9] C. Gabarró, J. Font, A. Camps, and M. Vall-Llossera, "Retrieved sea surface salinity and wind speed from L-band measurements for WISE and EUROSTARRS campaigns," in *Proc. EuroSTARRS, WISE LOSAC 1st Results Workshop*, 2003, pp. 163–171.
- [10] R. Panciera *et al.*, "The NAFE'05/CoSMOS data set: Toward SMOS soil moisture retrieval, downscaling, and assimilation," *IEEE Trans. Geosci. Remote Sens.*, vol. 46, no. 3, pp. 736–745, Mar. 2008.
- [11] R. Panciera *et al.*, "The Soil Moisture Active Passive Experiments (SMAPEX): Toward soil moisture retrieval from the SMAP mission," *IEEE Trans. Geosci. Remote Sens.*, vol. 52, no. 1, pp. 490–507, Jan. 2014.
- [12] M. Zribi *et al.*, "CAROLS: A new airborne L-band radiometer for ocean surface and land observations," *Sensors*, vol. 11, no. 1, pp. 719–742, Jan. 2011.
- [13] F. Baup, E. Mougin, P. De Rosnay, F. Timouk, and I. Chênerie, "Surface soil moisture estimation over the AMMA Sahelian site in Mali using ENVISAT/ASAR data," *Remote Sens. Environ.*, vol. 109, no. 4, pp. 473–481, Aug. 2007.
- [14] M. Shimada, O. Isoguchi, T. Tadono, and K. Isono, "PALSAR radiometric and geometric calibration," *IEEE Trans. Geosci. Remote Sens.*, vol. 47, no. 12, pp. 3915–3932, Dec. 2009.
- [15] T. J. Jackson, "Multiple resolution analysis of L-band brightness temperature for soil moisture," *IEEE Trans. Geosci. Remote Sens.*, vol. 39, no. 1, pp. 151–164, Jan. 2001.
- [16] I. E. Mladenova, T. J. Jackson, R. Bindlish, and S. Hensley, "Incidence angle normalization of radar backscatter data," *IEEE Trans. Geosci. Remote Sens.*, vol. 51, no. 3, pp. 1791–1804, Mar. 2013.
- [17] R. H. Reichle and R. D. Koster, "Bias reduction in short records of satellite soil moisture," *Geophys. Res. Lett.*, vol. 31, no. 19, pp. 1–4, Oct. 2004.
- [18] E. N. Anagnostou, A. J. Negri, and R. F. Adler, "Statistical adjustment of satellite microwave monthly rainfall estimates over Amazonia," *J. Appl. Meteorol.*, vol. 38, no. 11, pp. 1590–1598, Nov. 1999.
- [19] D. Atlas, D. Rosenfeld, and D. B. Wolff, "Climatologically tuned reflectivity-rain rate relations and links to area-time integrals," *J. Appl. Meteorol.*, vol. 29, no. 11, pp. 1120–1135, Nov. 1990.
- [20] Y. Y. Liu, A. I. van Dijk, R. A. de Jeu, and T. R. Holmes, "An analysis of spatiotemporal variations of soil and vegetation moisture from a 29-year satellite-derived data set over mainland Australia," *Water Resources Res.*, vol. 45, no. 7, pp. 1–12, Jul. 2009.
- [21] C. Menges, J. Van Zyl, G. Hill, and W. Ahmad, "A procedure for the correction of the effect of variation in incidence angle on AIRSAR data," *Int. J. Remote Sens.*, vol. 22, no. 5, pp. 829–841, 2001.
- [22] C. H. Menges, G. J. Hill, W. Ahman, and J. J. van Zyl, "Incidence angle correction of AIRSAR data to facilitate land-cover classification," *Photogramm. Eng. Remote Sens.*, vol. 67, no. 4, pp. 479–490, Apr. 2001.
- [23] S. Peischl *et al.*, "The AACES field experiments: SMOS calibration and validation across the Murrumbidgee River catchment," *Hydrol. Earth Syst. Sci. Discussions*, vol. 9, pp. 2763–2795, 2012.
- [24] C. Rudiger *et al.*, "Toward vicarious calibration of microwave remote-sensing satellites in arid environments," *IEEE Trans. Geosci. Remote Sens.*, vol. 52, no. 3, pp. 1749–1760, Dec. 2014.
- [25] Y. H. Kerr *et al.*, "The SMOS mission: New tool for monitoring key elements of the global water cycle," *Proc. IEEE*, vol. 98, no. 5, pp. 666–687, May 2010.
- [26] D. Entekhabi *et al.*, "The Soil Moisture Active Passive (SMAP) mission," *Proc. IEEE*, vol. 98, no. 5, pp. 704–716, May 2010.
- [27] J.-P. Wigneron *et al.*, "L-band Microwave Emission of the Biosphere (L-MEB) model: Description and calibration against experimental data sets over crop fields," *Remote Sens. Environ.*, vol. 107, no. 4, pp. 639–655, Apr. 2007.

- [28] J.-P. Wigneron, L. Laguerre, and Y. H. Kerr, "A simple parameterization of the L-band microwave emission from rough agricultural soils," *IEEE Trans. Geosci. Remote Sens.*, vol. 39, no. 8, pp. 1697–1707, Aug. 2001.
- [29] T. Mo, B. Choudhury, T. Schmugge, J. Wang, and T. Jackson, "A model for microwave emission from vegetation-covered fields," *J. Geophys. Res., Oceans*, vol. 87, no. C13, pp. 11229–11237, Dec. 1982.
- [30] T. Jackson and T. Schmugge, "Vegetation effects on the microwave emission of soils," *Remote Sens. Environ.*, vol. 36, no. 3, pp. 203–212, 1991.
- [31] A. A. Van de Griend and J.-P. Wigneron, "The B-factor as a function of frequency and canopy type at H-polarization," *IEEE Trans. Geoscience and Remote Sensing*, vol. 42, no. 4, pp. 786–794, Apr. 2004.
- [32] J. Wang and B. Choudhury, "Remote sensing of soil moisture content, over bare field at 1.4 GHz frequency," *J. Geophys. Res., Oceans*, vol. 86, no. C6, pp. 5277–5282, Jun. 1981.
- [33] M. C. Dobson, F. T. Ulaby, M. T. Hallikainen, and M. A. El-Rayes, "Microwave dielectric behavior of wet soil-Part II: Dielectric mixing models," *IEEE Trans. Geosci. Remote Sens.*, vol. GE-23, no. 1, pp. 35–46, Jan. 1985.



Nan Ye received the B.E. degree in hydraulic and hydropower engineering from Tsinghua University, Beijing, China, in 2006, and the Ph.D. degree in civil engineering from Monash University, Melbourne, Australia, in 2014.

In 2013, he was a Research Assistant with the Department of Geographic Information Science, Nanjing University, Nanjing, China. He is currently a Research Fellow with Monash University. His research interests include retrieval of soil moisture and snow properties from microwave observations.



Jeffrey P. Walker received the B.Eng.(Civil) and B.Surv. degrees (Hons. 1 and University Medal) from the University of Newcastle, Newcastle, Australia, in 1995, and the Ph.D. degree in water resources engineering from the University of Newcastle, in 1999.

He then joined the NASA Goddard Space Flight Center to implement his soil moisture work globally. In 2001, he moved to the Department of Civil and Environmental Engineering, University of Melbourne, Melbourne, Australia, as a Lecturer, where he continued soil moisture work, including development of the only Australian airborne capability for simulating new satellite missions for soil moisture. In 2010, he was appointed as a Professor with the Department of Civil Engineering, Monash University, Melbourne, Australia, where he is continuing this research. He is contributing to soil moisture satellite missions at NASA, ESA, and JAXA, as a Science Team Member for the Soil Moisture Active Passive (SMAP) mission and calibration/validation Team Member for the Soil Moisture and Ocean Salinity (SMOS), and Global Change Observation Mission-Water (GCOM-W), respectively.



Christoph Rüdiger (M'10) received the B.E. degree in civil engineering from the University of Applied Sciences, Wiesbaden, Germany, in 2002, and the Ph.D. degree in environmental engineering from the University of Melbourne, Melbourne, Australia, in 2007.

Currently, he is a Lecturer with Monash University, Melbourne, Australia. In 2007, he joined the Centre National de Recherches Météorologiques (CNRM), Météo France, Toulouse, France, to work on the preparation of surface soil moisture and LAI data assimilation into the French land surface model ISBA. Since his return to Australia in July 2008, he has coordinated and led a number of calibration/validation campaigns for the Australian land validation segment of SMOS mission in the Australian arid zone and the Murrumbidgee River catchment. In addition to this, he continues to work on land surface data assimilation and also participates in the Australian calibration/validation segments for NASA's SMAP and Aquarius. His research interests include remote sensing of vegetation dynamics and landscape water content.